

Coherent Josephson qubit suitable for scalable quantum integrated circuits

R. Barends,^{1,*} J. Kelly,^{1,*} A. Megrant,¹ D. Sank,¹ E. Jeffrey,¹ Y. Chen,¹ Y. Yin,^{1,†} B. Chiaro,¹ J. Mutus,¹ C. Neill,¹ P. O'Malley,¹ P. Roushan,¹ J. Wenner,¹ T. C. White,¹ A. N. Cleland,¹ and John M. Martinis¹

¹*Department of Physics, University of California, Santa Barbara, CA 93106, USA*

(Dated: April 9, 2013)

We demonstrate a planar, tunable superconducting qubit with energy relaxation times up to $44 \mu\text{s}$. This is achieved by using a geometry designed to both minimize radiative loss and reduce coupling to materials-related defects. At these levels of coherence, we find a fine structure in the qubit energy lifetime as a function of frequency, indicating the presence of a sparse population of incoherent, weakly coupled two-level defects. This is supported by a model analysis as well as experimental variations in the geometry. Our ‘Xmon’ qubit combines facile fabrication, straightforward connectivity, fast control, and long coherence, opening a viable route to constructing a chip-based quantum computer.

One of the outstanding challenges in building a quantum computer is to balance coherence, connectivity and control in the qubits. Superconductivity provides an appealing platform because it allows for scalability: the conduction electrons condense into a macroscopic quantum state, and large quantum integrated circuits can be made with many elements having individual control lines. However, quantum coherence in superconducting circuits has proven to be very delicate, as it is easily disturbed by material defects, electron system excitations, and radiative coupling to external wiring [1–7]. To minimize these and other effects, many groups have recently begun embedding qubits in three-dimensional superconducting cavities. These 3D qubits show high coherence, with energy relaxation times in 3D transmon qubits between 30 and $140 \mu\text{s}$ [8, 9].

Here, we demonstrate a new design for a fully planar superconducting qubit, based on the planar transmon [10, 11], with energy coherence times in excess of $40 \mu\text{s}$. Our approach balances coherence, connectivity, as well as fast control. We design the qubit with high-quality coplanar waveguide capacitors, motivated by the recent advances with superconducting resonators, yielding a modular design with straightforward connectivity. The qubits are frequency-tunable, which allows the implementation of fast two-qubit gates: a controlled-Z gate [12–14] can then be implemented with high fidelity in 25 ns [15]. With the coherence time exceeding single and two-qubit gates times by three orders of magnitude, we believe that our device provides a key ingredient for implementing a surface code quantum computer [16].

We also find that the small remnant decoherence in these qubits comes from a sparse bath of weakly coupled, incoherent defects. These defects are clearly visible in the measured quantum time-resolved spectroscopy, and give rise to frequency-dependent variations in the energy relaxation rate. These results may also explain the variations observed in lifetimes of 3D transmon qubits. We elucidate this physics and improve the coherence by varying the capacitor geometry.

Our device is shown in Fig. 1a, formed by patterning the Al metal (light), exposing the sapphire substrate (dark). The qubit is the cross-shaped device. Its four arms connect to separate elements, each having a different function: a coplanar waveguide resonator for readout on the top, a quantum bus resonator on the right to mediate coupling to other qubits, XY control on the left to excite the qubit state, and Z control on the bottom to tune the qubit frequency. The cross is the qubit capacitor, which connects at the bottom to the tunable Josephson superconducting quantum interference device (SQUID), see Fig. 1b. The rectangular ring is intersected by two iden-

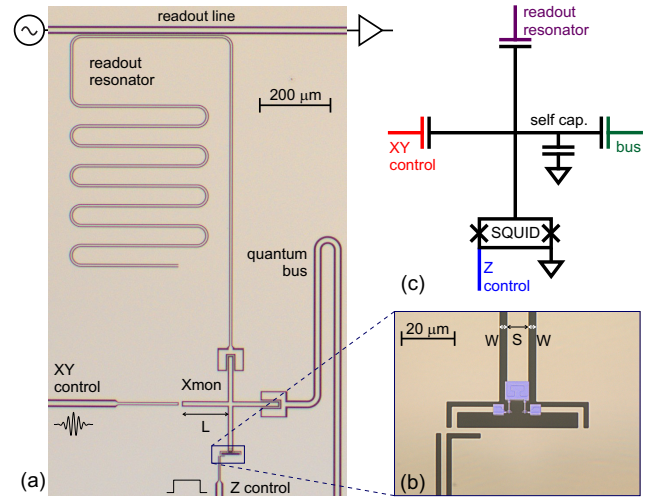


FIG. 1: (Color online) (a) Optical micrograph of the planar ‘Xmon’ qubit, formed by the Al superconducting film (light) and the exposed sapphire substrate (dark). The qubit is capacitively coupled to a quarter wave readout resonator (top), a quantum bus resonator (right), a XY control line (left), and inductively coupled to a Z control line (bottom). The Xmon arm length is L . (b) The inset shows the shadow evaporated Al junction layer in false color (blue). The junction size is $0.30 \times 0.20 \mu\text{m}^2$. The capacitor central linewidth is S , the gap width is W . (c) The electrical circuit of the qubit.

tically sized Al tunnel junctions (blue in Fig. 1b). The electrical circuit is equivalent to that of a grounded transmon [10], with the capacitor in parallel with the tunable junction (Fig. 1c). In a clear departure from the traditional floating transmon with an interdigitated capacitor (IDC) [11], we chose to form the qubit capacitor by intersecting two coplanar waveguide lines.

In prior work, we showed that highly coherent coplanar waveguide resonators can be fabricated, having quality factors of about 1.5×10^6 at the single photon occupation level. These resonators were made from molecular beam epitaxy (MBE) Al on oxygen-cleaned sapphire [17]. This shows that a straightforward path to high coherence comes from a combination of I) MBE Al as high quality material, II) coplanar waveguides having low radiative loss, and III) embedding in a groundplane. We therefore embed the qubit in an uninterrupted groundplane, with thin Al lines at the capacitor ends tying the groundplanes together; this suppresses parasitic slotline modes in the control lines and resonators as well.

Connectivity is accomplished by coupling each of the qubit's arms to a distinct element with specific functionality. Three of the connections are easily made with a coupling capacitor, as the qubit is connected to ground. An advantage of this approach is that each coupling can be individually tuned and optimized. To this end, we have also separated out qubit control. The XY control drive line is connected with a coupling $C_c = 60$ aF, which allows us to excite the qubit state in 10 ns but hardly affects coherence, with an estimated T_1 of 0.3 ms. The Z control also combines speed and coherence. The drive line is galvanically connected to the SQUID to allow for a large inductive coupling with a mutual inductance of $M = 2.2$ pH. We are able to rapidly detune the qubit on the timescale of a nanosecond [18]. The measured parasitic coupling between the Z line and the qubit gives an estimated T_1 of ~ 30 ms [19].

The qubit design outlined above balances coherence, control and connectivity in the qubit, using a robust design for the capacitor and a modular separation of functionality. Our approach differs on key points from previous implementations. With this experimental nature in mind, we name our qubit the 'Xmon'. While the cross-shaped qubit capacitor may emphasize this name, more arms can be added to allow for more connectivity.

We find a dramatic increase in Xmon energy coherence compared to the traditional planar transmon, measuring decay times up to $T_1 = 44 \mu\text{s}$, see Fig. 2a. The qubit T_1 is measured by exciting it with a π -pulse, and measuring its state after a variable time $\Delta\tau$. We find that the excited state probability decays exponentially. We find Ramsey and spin echo phase coherence times up to $T_2^* = 15 \mu\text{s}$ and $T_2 = 20 \mu\text{s}$ at the flux insensitive point, respectively, see Fig. 2b. The energy decay at this point is measured to be $T_1 = 18 \mu\text{s}$. The dephasing envelopes are measured using tomography. The first pulse is $X_{\pi/2}$,

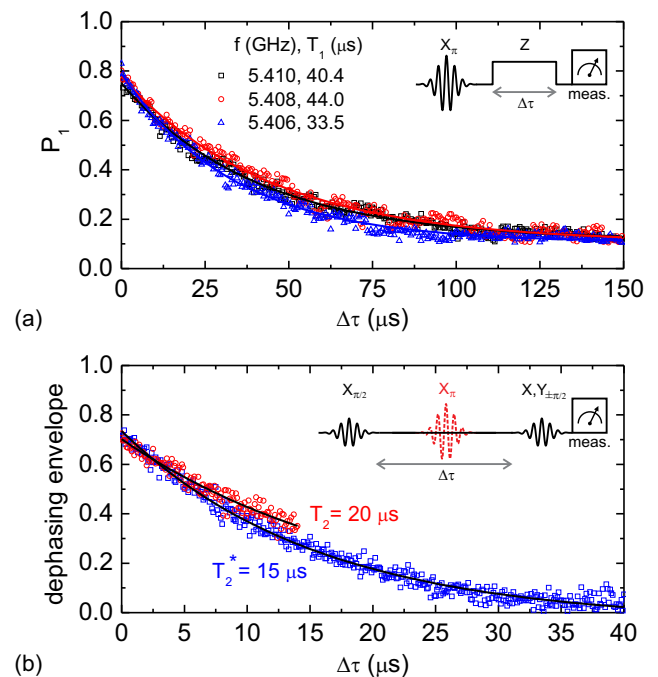


FIG. 2: (Color online) (a) Qubit energy decay at three nearby frequencies. The qubit frequency is adjusted by applying a rectangular pulse with length $\Delta\tau$ on the Z line. The pulse sequence is shown in the inset. (b) Ramsey T_2^* and spin echo T_2 dephasing envelopes at the flux insensitive point, measured by phase tomography. The inset shows the pulse sequence; for the spin echo we apply a refocussing pulse (dashed). We apply four phases to the last pulse for phase tomography, to measure the decay envelope. Spin echo measurements are limited by electronics to $14 \mu\text{s}$. The energy coherence for the dephasing measurement was $T_1 = 18 \mu\text{s}$.

followed by $X_{\pi/2}$, $X_{-\pi/2}$, $Y_{\pi/2}$, or $Y_{-\pi/2}$ (see inset for the pulse sequence), producing fringes with different phases. The dephasing envelopes follow an exponential decay. As the limit of $T_2 = 2T_1$ has not been reached [10], this indicates the presence of an additional dephasing channel. This channel, as well as dephasing away from the flux insensitive point, is presently under investigation.

The qubits used here had ground to excited state transition frequencies around 6 GHz when unbiased, nonlinearities around 230 MHz, and a ratio of Josephson to charging energy $E_J/E_C \sim 95$. We employ a dispersive, high-power single-shot readout scheme with a 70-85% fidelity [20]. The readout resonator frequencies used are 6.4-6.7 GHz, the loaded quality factor is $Q_l = 10^4$, and the resonator-qubit coupling strength is approximately 40 MHz. Measurements were done in a dilution refrigerator with a base temperature of 30 mK, with multistage infrared shielding [21]. Magnetic fields were reduced by room temperature and cryogenic magnetic shields, with nonmagnetic microwave connectors [22].

The results in Fig. 2 show that tunable superconducting qubits with a planar geometry can have T_1 values in

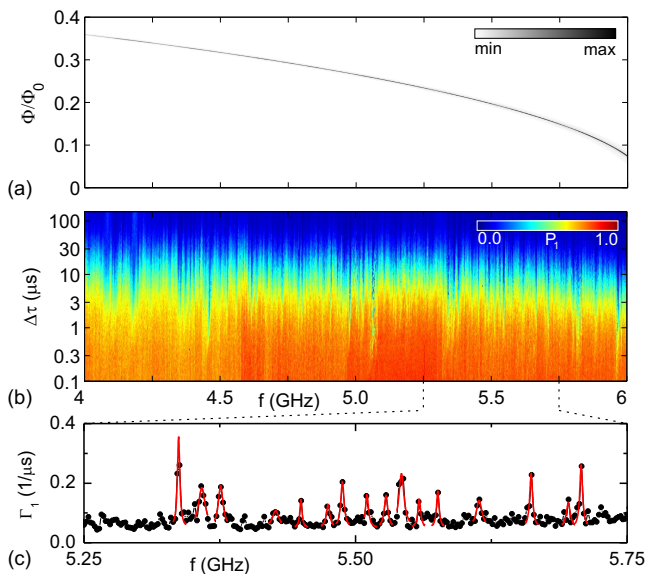


FIG. 3: (Color online) (a) Qubit spectroscopy for device with $S, W = 8, 8 \mu\text{m}$. A smooth curve is formed by the high transmission (grey), measured on resonance with the readout resonator, which indicates when the qubit is excited. (b) Swap spectroscopy of the same qubit. The qubit is detuned from 4 to 6 GHz (stepsize 2 MHz), and the delay time is varied from 100 ns to 150 μs . See the inset of Fig. 2a for the pulse sequence. (c) Qubit relaxation rate at qubit frequencies from 5.25 to 5.75 GHz, extracted from the data in (b). Sharp peaks above a background are observed. The peaks are fitted to Eq. 1 (solid lines).

excess of 40 μs . In fact, this T_1 corresponds to the MBE Al resonator quality factors [17], for which $T_1 = Q/\omega$ is also about 40 μs . The combination of long energy and phase coherence times compare well with previously reported values for planar superconducting Al qubits: for transmons $T_1 = 9.7 \mu\text{s}$ and $T_2^* = 10 \mu\text{s}$ [23], for charge qubits $T_1 = 200 \mu\text{s}$ and $T_2^* = 0.07 \mu\text{s}$ [24], for flux qubits $T_1 = 12 \mu\text{s}$ and $T_2^* = 2.5 \mu\text{s}$ [25], and for the fluxonium $T_1 = 10 \mu\text{s}$ and $T_2^* = 2 \mu\text{s}$ [26]. In fact, the Xmon approaches the long coherence found in 3D transmons [8, 9]. Very recently, TiN planar devices have shown long coherence [27, 28], encouraging using Xmon geometries with this material.

We find that the energy relaxation depends on qubit frequency, as we observe different exponential decay rates for small changes in frequency. As shown in Fig. 2a, we find T_1 values from 34 to 44 μs in a 4 MHz band near 5.4 GHz. In order to elucidate this further, we performed a spectroscopic scan on the qubit, shown in Fig. 3a. The qubit frequency displays the expected dependence on applied flux Φ [10], varying smoothly without visible splittings, indicating that strongly coupled defects, which manifest as avoided level crossings [1], are virtually absent. We then performed a quantum analogue of time-resolved spectroscopy (swap spectroscopy [29]), shown in

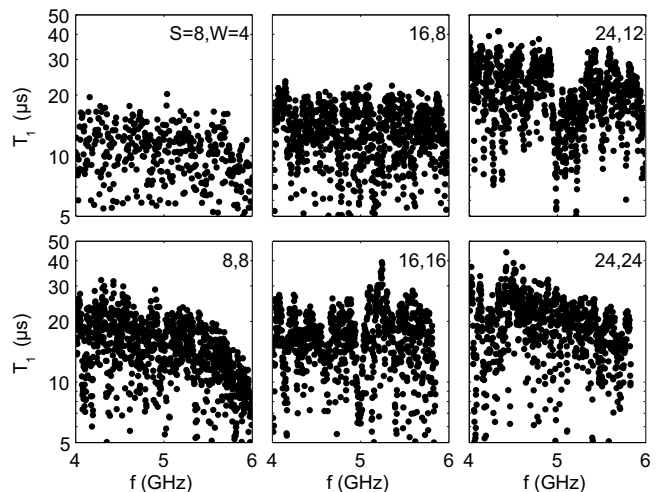


FIG. 4: Frequency dependence of T_1 for six qubits with different S and W (see Table I). The frequency stepsize is 5 MHz for $S, W = 8, 4 \mu\text{m}$ and 2 MHz otherwise. See Supplementary Material [18] for the corresponding decay rates.

Fig. 3b. The probability of the excited state (color) is plotted for $\Delta\tau$ from 100 ns to 150 μs (logarithmic vertical scale) and qubit frequencies from 4 to 6 GHz. We find that the probability decays exponentially, but with a fine structure of variable energy relaxation, and distinct peaks in the energy decay rate (Fig. 3c). We do not observe any chevron interference patterns [29], implying no defects interact coherently with the qubit state. After cycling the temperature to 4.2 K the fine structure is altered, but the overall image remains unchanged. We count approximately 30 regions with reduced coherence ($T_1 < 8 \mu\text{s}$) per GHz in Fig. 3b.

We explored the dependence of the qubit coherence time on capacitor geometry, using six different qubit capacitor designs; the central line width S , gap width W and arm length L were varied, while the capacitance value [30] and junction parameters are kept the same. The parameters are listed in Table I; see Supplementary Material [18] for a micrograph. We find that the swap spectroscopy measurements of the different designs share the same characteristics as shown in Fig. 3b: a fine structure with varying exponential decay. The energy relaxation times extracted from the measurements are shown

TABLE I: Geometric parameters for the Xmon qubit capacitors as defined in Fig. 1 along with their frequencies. Groups of three qubits indicate that the devices are on the same chips.

S (μm)	8	16	24	8	16	24
W (μm)	4	8	12	8	16	24
L (μm)	130	130	130	165	165	165
$f_{10,\text{max}}$ (GHz)	6.094	6.158	6.071	6.080	5.883	5.846
nonlinearity (MHz)	224	228	222	220	225	223

in Fig. 4. With larger capacitor size the overall energy relaxation time increases: when changing S, W from $8, 4 \mu\text{m}$ to $16, 8 \mu\text{m}$ and $24, 12 \mu\text{m}$, the T_1 improves from a band of values between 8-15 to 10-20, and 20-40 μs , respectively. Importantly, both the upper as well the lower bounds on T_1 increase with capacitor width. This is repeated in the qubits with S, W ranging from $8, 8 \mu\text{m}$ to $16, 16 \mu\text{m}$ and $24, 24 \mu\text{m}$. The reduction of T_1 at frequencies approaching 6 GHz is due to Purcell decay into the readout resonator [31]. We emphasize that these T_1 values are obtained in multiqubit chips including complete sets of control wiring.

The improvement of T_1 with increasing width is consistent with previous experiments on superconducting resonators [32, 33]. Loss arises from the electric fields coupling to two-level systems with dipole moments [34], which reside predominantly in surface oxides and interfaces. This loss depends on the participation ratio, which depends on the electric field distribution [35]. Widening the capacitor reduces the participation of the surfaces and thus the loss, a natural explanation for the approximately linear increase in average T_1 with width in Fig. 4. On the other hand, the peaks in the decay rate are reminiscent of experiments with phase qubits [1], where localized features in the frequency dependence occur when the qubit couples strongly to two-level defects, often giving rise to splitting of the qubit frequency and the chevron-shaped signature of coherent swapping. However, the exponential decay in the Xmon qubit, with no signatures of swapping or splitting, suggests a different energy relaxation mechanism.

Here, we show how surface defects near the metal edges of the capacitor provide a natural explanation for the peaks in the energy decay. The key point is that loss arises from the qubit interacting with a sparse bath of incoherent defects, as indicated by our data: the sharp frequency dependence as well as the changes in fine structure when cycling to 4.2 K are both clear indicators of defects. The absence of chevrons and qubit frequency splittings correspond to incoherent interaction. The lower and upper bounds of T_1 increasing with capacitor dimension indicates the defects reside in the capacitor.

We model a quantum system consisting of a qubit, with a frequency-independent background loss rate $\Gamma_{1,Q}$ and pure dephasing rate $\Gamma_{\phi,Q}$, and a single two-level defect with decoherence rate $\Gamma_{1,D}$ and dephasing rate $\Gamma_{\phi,D}$ (see Supplementary Material [18]). When the defect decoherence rate exceeds the coupling strength g , coherent swapping vanishes and an incoherent, exponential decay appears. From a two-spin Hamiltonian (see Supplementary Material), we derive the qubit energy relaxation rate Γ_1 (in the limit $\Gamma_{1,D} > g > \Gamma_{1,Q}$) to be

$$\Gamma_1 = \frac{2g^2\Gamma}{\Gamma^2 + \Delta^2} + \Gamma_{1,Q}, \quad (1)$$

with detuning Δ , and $\Gamma = \Gamma_{1,D}/2 + \Gamma_{\phi,D} + \Gamma_{1,Q}/2 + \Gamma_{\phi,Q}$.

Hence, each uncorrelated defect adds a single Lorentzian to the energy decay rate. We can roughly estimate the coupling strength g for a surface defect with dipole moment $p \sim 1 \text{ D}$ at a distance x away from the metal edge. With the electric field given by $E = B/\sqrt{x}$ [36], and B from numerical simulations [37], we arrive at $g/2\pi \sim 0.1 \text{ MHz}$ ($g = pE$) for a defect located at $x = 3 \text{ nm}$ away from the metal. We apply our model to Fig. 3c and find that the peaks in decay rate can be described by a set of Lorentzians, with $1/(\Gamma_{1,D}/2 + \Gamma_{\phi,D}) \sim 50 - 100 \text{ ns}$, consistent with defect decay rates measured in similar systems [1, 38], and with $g/2\pi \gtrsim 0.2 \text{ MHz}$, agreeing with incoherent loss.

We can also estimate the number of individually resolvable defects using two-level system physics developed for junctions. The substrate-metal interface in our devices was thoroughly cleaned [17], hence we assume that the bulk of strongly-coupled defects resides in the metal- and substrate-air interfaces, as they have the highest participation ratios [35]. The defect density for AlO_x in tunnel barriers has been established in measurements with phase qubits [1], with the distribution over dipole moment given by $\rho_0 \sqrt{1 - p^2/p_{\text{max}}^2}/p$, with $\rho_0 \approx 10^2/\mu\text{m}^3/\text{GHz}$, and the maximum dipole moment $p_{\text{max}} = 6 \text{ D}$. We take these numbers as representative and assume a 3 nm thick dielectric layer with defects [39]. The number of defects with coupling strength greater than g_{min} is then given by

$$N = \iint \rho_0 \frac{\sqrt{1 - p^2/p_{\text{max}}^2}}{p} \Theta[p|E(\vec{r})| - g_{\text{min}}] dp d\vec{r}, \quad (2)$$

with Θ the unit step function and $E(\vec{r})$ the electric field at position \vec{r} . Simulations using Eq. 2 as well as Monte Carlo simulations indicate $N \sim 30 - 50/\text{GHz}$, for $g_{\text{min}}/2\pi \sim 0.2 \text{ MHz}$. We emphasize that the simulations connect g_{min} to N with values which are close to what is observed experimentally. The Monte Carlo simulations (see Supplementary Material [18]) also indicate that the bulk of strongly coupled defects reside within a $\sim 100 \text{ nm}$ distance from the etched metal edges, where the electric fields are largest. In addition, we have simulated the qubit decay rate (see Supplementary Material), reproducing the experimentally observed features: the simulated decay rate shows both the peaks as well as the variation in the background.

The good quantitative comparison between model and experiment gives compelling evidence that a sparse bath of incoherent defects plays a major role in loss in highly coherent qubits. Our results may also explain previously reported anomalous behavior in planar transmon qubits with long coherence, for which the T_1 has been reported to vary significantly between qubits, even on the same chip [23, 40]. This is consistent with a sparse bath of incoherent defects limiting the coherence, as in Fig. 3.

In conclusion, we demonstrate energy coherence times exceeding 40 μs in tunable, planar superconducting qubits. We have achieved this using a geometry with

low radiative dissipation and high quality materials. At these high coherence levels we identify a novel decoherence mechanism, loss from a sparse bath of incoherent defects, which is apparent in the swap spectroscopy. We show how enlarging the capacitor improves coherence. Our qubits combine long coherence, easy interconnectivity, and fast control, providing a key ingredient for the implementation of an on-chip surface code quantum computer.

This work was supported by the Rubicon program of the Netherlands Organisation for Scientific Research (NWO), and the Office of the Director of National Intelligence (ODNI), Intelligence Advanced Research Projects Activity (IARPA), through the Army Research Office grants W911NF-09-1-0375 and W911NF-10-1-0334. All statements of fact, opinion or conclusions contained herein are those of the authors and should not be construed as representing the official views or policies of IARPA, the ODNI, or the U.S. Government. Devices were made at the UC Santa Barbara Nanofabrication Facility, a part of the NSF-funded National Nanotechnology Infrastructure Network, and at the NanoStructures Cleanroom Facility.

* These authors contributed equally to this work.

† Present address: Department of Physics, Zhejiang University, Hangzhou 310027, China

- [1] J. M. Martinis, K. B. Cooper, R. McDermott, M. Steffen, M. Ansmann, K. Osborn, K. Cicak, S. Oh, D. P. Pappas, R. W. Simmonds, C. C. Yu, Phys. Rev. Lett. **95**, 210503 (2005).
- [2] G. J. Grabovskij, T. Peichl, J. Lisenfeld, G. Weiss, A. V. Ustinov, Science **338**, 232 (2012).
- [3] J. Wenner, Y. Yin, E. Lucero, R. Barends, Y. Chen, B. Chiaro, J. Kelly, M. Lenander, M. Mariantoni, A. Megrant, C. Neill, P. J. J. O'Malley, D. Sank, A. Vainsencher, H. Wang, T. C. White, A. N. Cleland, J. M. Martinis, accepted for publication in Phys. Rev. Lett. (2013).
- [4] G. Catelani, S. E. Nigg, S. M. Girvin, R. J. Schoelkopf, and L. I. Glazman, Phys. Rev. B **86**, 184514 (2012).
- [5] D. Ristè, C. C. Bultink, M. J. Tiggelman, R. N. Schouten, K. W. Lehnert, and L. DiCarlo, arXiv:1212.5459.
- [6] M. D. Shaw, R. M. Lutchyn, P. Delsing, and P. M. Echternach, Phys. Rev. B **78**, 024503 (2008).
- [7] P. Lafarge, P. Joyez, D. Esteve, C. Urbina, M. H. Devoret, Phys. Rev. Lett. **70**, 994 (1993).
- [8] H. Paik, D. I. Schuster, L. S. Bishop, G. Kirchmair, G. Catelani, A. P. Sears, B. R. Johnson, M. J. Reagor, L. Frunzio, L. I. Glazman, S. M. Girvin, M. H. Devoret, R. J. Schoelkopf Phys. Rev. Lett. **107**, 240501 (2011),
- [9] C. Rigetti, J. M. Gambetta, S. Poletto, B. L. T. Plourde, J. M. Chow, A. D. Córcoles, J. A. Smolin, S. T. Merkel, J. R. Rozen, G. A. Keefe, M. B. Rothwell, M. B. Ketchen, and M. Steffen, Phys. Rev. B **86**, 100506 (2012).
- [10] J. Koch, T. M. Yu, J. Gambetta, A. A. Houck, D. I. Schuster, J. Majer, A. Blais, M. H. Devoret, S. M. Girvin, and R. J. Schoelkopf, Phys. Rev. A **76**, 042319 (2007).
- [11] A. A. Houck, D. I. Schuster, J. M. Gambetta, J. A. Schreier, B. R. Johnson, J. M. Chow, L. Frunzio, J. Majer, M. H. Devoret, S. M. Girvin, and R. J. Schoelkopf, Nature **449**, 328 (2007).
- [12] F. W. Strauch, P. R. Johnson, A. J. Dragt, C. J. Lobb, J. R. Anderson, and F. C. Wellstood, Phys. Rev. Lett. **91**, 167005 (2003).
- [13] L. DiCarlo, J. M. Chow, J. M. Gambetta, Lev S. Bishop, B. R. Johnson, D. I. Schuster, J. Majer, A. Blais, L. Frunzio, S. M. Girvin and R. J. Schoelkopf, Nature **460**, 240 (2009).
- [14] M. Mariantoni, H. Wang, T. Yamamoto, M. Neeley, R. C. Bialczak, Y. Chen, M. Lenander, E. Lucero, A. D. O'Connell, D. Sank, M. Weides, J. Wenner, Y. Yin, J. Zhao, A. N. Korotkov, A. N. Cleland, J. M. Martinis, Science **334**, 61 (2011).
- [15] J. Ghosh, A. Galiutdinov, Z. Zhou, A. N. Korotkov, J. M. Martinis, M. R. Geller, Phys. Rev. A **87**, 022309 (2013).
- [16] A. G. Fowler, M. Mariantoni, J. M. Martinis, A. N. Cleland, Phys. Rev. A **86**, 032324 (2012).
- [17] A. Megrant, C. Neill, R. Barends, B. Chiaro, Y. Chen, L. Feigl, J. Kelly, E. Lucero, M. Mariantoni, P. J. J. O'Malley, D. Sank, A. Vainsencher, J. Wenner, T. C. White, Y. Yin, J. Zhao, C. J. Palmström, J. M. Martinis, A. N. Cleland, Appl. Phys. Lett. **100**, 113510 (2012).
- [18] See Supplementary Material at [weblink will be inserted by editor].
- [19] We measure the effective inductive coupling between qubit and inductive driveline [10] to be $M' = 0.1$ pH.
- [20] M. D. Reed, L. DiCarlo, B. R. Johnson, L. Sun, D. I. Schuster, L. Frunzio, and R. J. Schoelkopf, Phys. Rev. Lett. **105**, 173601 (2010).
- [21] R. Barends, J. Wenner, M. Lenander, Y. Chen, R. C. Bialczak, J. Kelly, E. Lucero, P. O'Malley, M. Mariantoni, D. Sank, H. Wang, T. C. White, Y. Yin, J. Zhao, A. N. Cleland, J. M. Martinis, J. J. A. Baselmans, Appl. Phys. Lett. **99**, 113507 (2011).
- [22] EZ Form Cable Corporation, Hamden, CT 06517 USA.
- [23] J. M. Chow, J. M. Gambetta, A. D. Corcoles, S. T. Merkel, J. A. Smolin, C. Rigetti, S. Poletto, G. A. Keefe, M. B. Rothwell, J. R. Rozen, M. B. Ketchen, and M. Steffen, Phys. Rev. Lett. **109**, 060501 (2012).
- [24] Z. Kim, B. Suri, V. Zaretsky, S. Novikov, K. D. Osborn, A. Mizel, F. C. Wellstood, and B. S. Palmer, Phys. Rev. Lett. **106**, 120501 (2011).
- [25] J. Bylander, S. Gustavsson, F. Yan, F. Yoshihara, K. Harrabi, G. Fitch, D. G. Cory, Y. Nakamura, J.-S. Tsai, W. D. Oliver, Nature Phys. **7**, 565 (2011).
- [26] V. Manucharyan, N. A. Masluk, A. Kamal, J. Koch, L. Glazman, M. H. Devoret, Phys. Rev. B. **85**, 024521 (2012).
- [27] J. Chang, M. R. Vissers, A. D. Corcoles, M. Sandberg, J. Gao, D. W. Abraham, J. M. Chow, J. M. Gambetta, M. B. Rothwell, G. A. Keefe, M. Steffen, D. P. Pappas, arXiv:1303.4071.
- [28] J. M. Sage, V. Bolkhovsky, W. D. Oliver, B. Turek, and P. B. Welander, J. Appl. Phys. **109**, 063915 (2011).
- [29] K. B. Cooper, M. Steffen, R. McDermott, R. W. Simmonds, S. Oh, D. A. Hite, D. P. Pappas, J. M. Martinis Phys. Rev. Lett. **93**, 180401 (2004).
- [30] The Xmon capacitance is closely approximated by the coplanar waveguide formula:

- $C = 8L(\epsilon_0 + \epsilon_{\text{sub}})K(k)/K(\sqrt{1-k^2})$, with ϵ_0 the vacuum permittivity, ϵ_{sub} the substrate permittivity, $k = S/(S + 2W)$, and K the complete elliptic integral.
- [31] A. A. Houck, J. A. Schreier, B. R. Johnson, J. M. Chow, J. Koch, J. M. Gambetta, D. I. Schuster, L. Frunzio, M. H. Devoret, S. M. Girvin, R. J. Schoelkopf. *Phys. Rev. Lett.* **101**, 080502 (2008).
- [32] R. Barends, N. Vercruyssen, A. Endo, P. J. de Visser, T. Zijlstra, T. M. Klapwijk, P. Diener, S. J. C. Yates, and J. J. A. Baselmans, *Appl. Phys. Lett.* **97**, 023508 (2010).
- [33] J. Gao, M. Daal, A. Vayonakis, S. Kumar, J. Zmuidzinas, B. Sadoulet, B. A. Mazin, P. K. Day, and Henry G. Leduc, *Appl. Phys. Lett.* **92**, 152505 (2008).
- [34] W. A. Phillips, *Rep. Prog. Phys.* **50**, 1657 (1987).
- [35] J. Wenner, R. Barends, R. C. Bialczak, Yu Chen, J. Kelly, Erik Lucero, Matteo Mariantoni, A. Megrant, P. J. J. O'Malley, D. Sank, A. Vainsencher, H. Wang, T. C. White, Y. Yin, J. Zhao, A. N. Cleland, John M. Martinis, *Appl. Phys. Lett.* **99**, 113513 (2011).
- [36] J. D. Jackson, *Classical Electrodynamics*, 3rd ed. (Wiley, Hoboken, 1999).
- [37] For the $S = 8$, $W = 8$ geometry, we find for the electric field away from the metal edge in the plane of the substrate surface: $E = B/\sqrt{x}$, with $B = 2 \text{ mV}/\sqrt{\text{m}}$.
- [38] Y. Shalibo, Y. Rofo, D. Shwa, F. Zeides, M. Neeley, J. M. Martinis, N. Katz, *Phys. Rev. Lett.* **105**, 177001 (2010).
- [39] Using a thickness of 2 nm instead of 3 nm for the dielectric layer does not significantly affect the outcome.
- [40] M. Sandberg, M. R. Vissers, T. Ohki, J. Gao, J. Aumentado, M. Weides, D. P. Pappas, arXiv:1211.2017.

Supplementary material for “Coherent Josephson qubit suitable for scalable quantum integrated circuits”

R. Barends,^{1,*} J. Kelly,^{1,*} A. Megrant,¹ D. Sank,¹ E. Jeffrey,¹ Y. Chen,¹ Y. Yin,^{1,†} B. Chiaro,¹ J. Mutus,¹ C. Neill,¹ P. O’Malley,¹ P. Roushan,¹ J. Wenner,¹ T. C. White,¹ A. N. Cleland,¹ and John M. Martinis¹

¹*Department of Physics, University of California, Santa Barbara, CA 93106, USA*

DEVICE FABRICATION

The devices were made in a two-step deposition process. The qubit capacitor, groundplane, readout resonator and control and readout wiring were made in a first, separate deposition step. We used molecular beam epitaxy (MBE) Al deposited on a *c*-plane sapphire substrate. The Al film thickness is approximately 100 nm, deposited at room temperature. The sapphire substrate was cleaned by load-lock outgassing at 200 °C, followed by heating to 850 °C in $\sim 10^{-6}$ Torr activated oxygen, identical to the process outlined in Ref. [1]. The first Al layer was patterned by a BCl_3/Cl_2 reactive ion etch.

In the final step, $0.30 \times 0.20 \mu\text{m}^2$ Al tunnel barriers (30 nm bottom and 100 nm top layer thickness) were made using double-angle shadow evaporation. We used

a high vacuum electron-beam evaporator, with a base pressure of approximately 5×10^{-8} Torr. We used the Dolan bridge technique with a poly(methyl methacrylate)/copolymer resist bilayer (approximate thickness: 0.30 and 0.50 μm , respectively), patterned with electron beam lithography. In order to make galvanic contact between the first Al layer and the junction layer, we used a 3 min long Ar ion mill (beam: 400 V, 21 mA; beam width: $\sim 3.2''$) before shadow-evaporation. Approximately 40 nm was removed from the top resist layer during the ion mill. The junctions were oxidized for 80 mins at 5.0 mBar. Lift-off was done in N-methyl-2-pyrrolidinone at 80 °C.

We find that the junctions age very little, the resistance value changes less than 1% over a period of ten days. An optical micrograph of the devices is shown in Fig. S1.

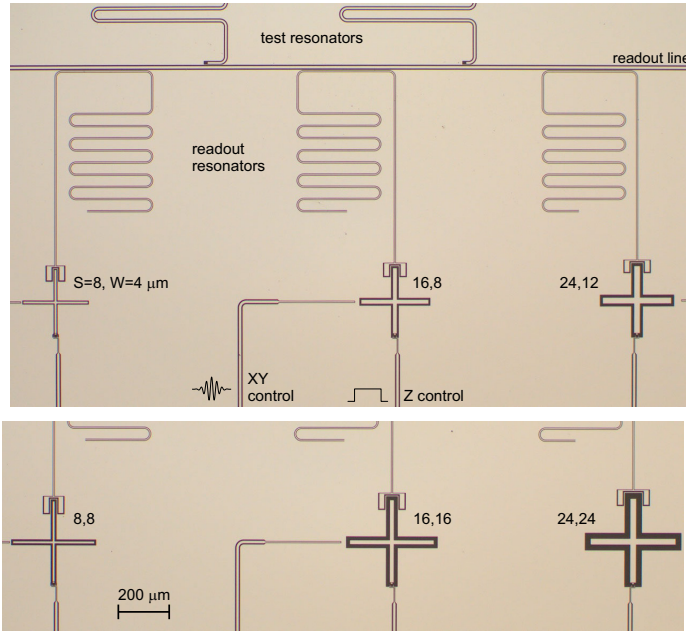


FIG. S1: (Color online) Optical micrograph of the six ‘Xmon’ qubits on two chips, formed by the Al superconducting (light) and the exposed sapphire substrate (dark). The qubits are capacitively coupled to readout resonators, which couple to a readout line in a frequency multiplexed readout scheme [2]. The central linewidth S and gap width W are varied from 8,4 μm to 24,24 μm . The top three Xmons have a single arm length of $L = 130 \mu\text{m}$, the bottom three have $L = 165 \mu\text{m}$. Test resonators provide an independent measurement of the quality factor.

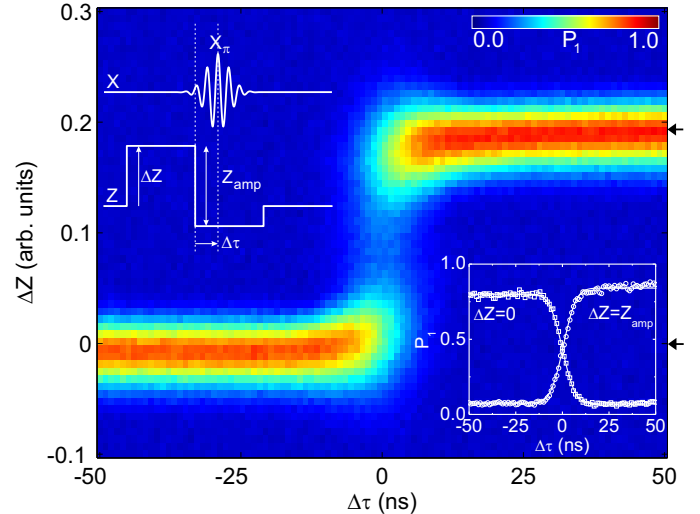


FIG. S2: (Color online) Z pulse shape measurement. The qubit is excited with a π -pulse with 20 ns Gaussian envelope, while a rectangular wave is applied on the Z line. The pulse sequence is shown in the left inset. We use $Z_{\text{amp}} = 0.2$ (arb. units) [3]. The right inset is a cross section at $\Delta Z = 0$ (squares) and $\Delta Z = Z_{\text{amp}}$ (circles), as indicated by the arrows (right). The solid lines are fits to partial qubit rotations from a π -pulse with a truncated Gaussian envelope.

Z PULSE

In order to quantify the response time of the qubit to a Z pulse, we simultaneously apply a π -pulse with a Gaussian envelope on the XY control and a rectangular wave pattern on the Z control line. The pulse sequence is shown in the left inset in Fig. S2. We slide the rectangular wave in time ($\Delta\tau$) and offset (ΔZ), while retaining the amplitude of the wave Z_{amp} constant. The excited state population is plotted in Fig. S2 as a function of time and amplitude.

A cross section of the main figure at $\Delta Z = 0$ (squares) and $\Delta Z = Z_{\text{amp}}$ (circles) is shown in the right inset. The measured response can be accurately described by qubit rotation from a partial π -pulse (π -pulse duration: 20 ns), with a truncated Gaussian as envelope (solid lines). No other time constants are included. We find that the rise at $\Delta Z = Z_{\text{amp}}$ is best described when assuming a 0.5 ns delay compared to the fall at $\Delta Z = 0$. We conclude that the qubit frequency is tuned to the desired frequency on a timescale of nanoseconds.

We find the Z control cross-talk between adjacent Xmons to be 1.0-1.5 %.

QUBIT DECAY RATE

The frequency-dependent decay rate for the six qubits, shown in Fig. S1, is displayed in Fig. S3.

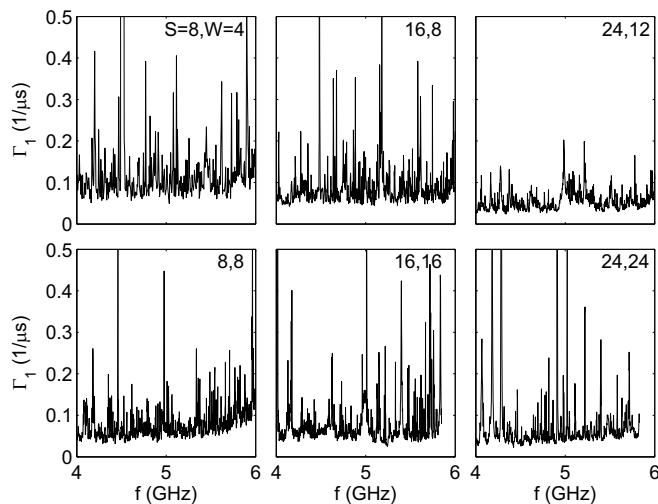


FIG. S3: Frequency dependence of Γ_1 for six qubits with different S and W . The frequency stepsize is 5 MHz for $S, W = 8, 4 \mu\text{m}$ and 2 MHz otherwise.

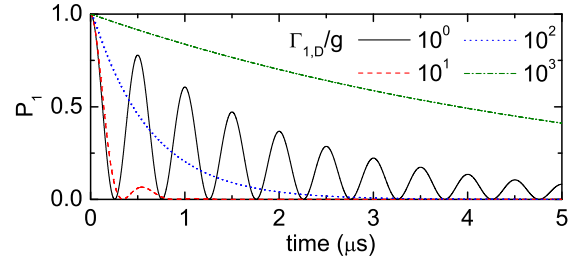


FIG. S4: (Color online) Qubit excited state probability versus time, in a simulation of a qubit-defect system. The qubit is on resonance with the defect, whose energy relaxation time is $\Gamma_{1,D}$. Here, we used a coupling strength $g/2\pi = 1$ MHz.

SIMULATION OF A QUBIT-DEFECT SYSTEM

In order to elucidate the crossover from coherent to incoherent decay of the qubit state, we numerically simulate a qubit-defect system. The system consists of two coupled two-level systems, with coupling strength g and defect energy decay rate $\Gamma_{1,D}$; the qubit is placed on resonance with the defect. The qubit excited state probability is shown in Fig. S4. For $\Gamma_{1,D} < g$, the excitation coherently swaps back and forth between qubit and defect, decaying slowly. When the decay rate exceeds the coupling strength ($\Gamma_{1,D} > g$) coherent swapping vanishes and an exponential decay appears, as the qubit state decays incoherently. Interestingly, the excitation decays most quickly for $\Gamma_{1,D} \approx g$.

ANALYTICAL EXPRESSION FOR LOSS IN A QUBIT-DEFECT SYSTEM

Here we derive an analytical expression for the energy loss rate arising from a qubit coupling to a single two-level defect. We consider a system with two coupled two-level systems. We solve the master equation in the Lindblad form,

$$\dot{\rho} = -\frac{i}{\hbar}[H, \rho] + \sum_i \mathcal{D}[C_i] \rho, \quad (\text{S1})$$

with $\mathcal{D}[C] \rho = C \rho C^\dagger - (C^\dagger C \rho + \rho C^\dagger C)/2$ and the Hamiltonian given by

$$H = \hbar\omega_Q a^\dagger a + \hbar\omega_D b^\dagger b + \hbar g (b^\dagger \otimes a + b \otimes a^\dagger), \quad (\text{S2})$$

with a and b the lowering operator for qubit and defect, respectively, and ω the radial transition frequency. We model Markovian decoherence through the Lindblad terms: $C_{i=1-4} = \{a\sqrt{\Gamma_{1,Q}}, a^\dagger a\sqrt{2\Gamma_{\phi,Q}}, b\sqrt{\Gamma_{1,D}}, b^\dagger b\sqrt{2\Gamma_{\phi,D}}\}$, denoting

energy and phase relaxation for qubit and defect, respectively. Here we used the number operators $a^\dagger a$ and $b^\dagger b$ to express pure dephasing, and $\Gamma_{1,Q}$ denotes qubit relaxation. We take $\Gamma_{1,Q} \ll \Gamma_{1,D}$. As we are interested in the relaxation of a single excitation, we only consider the states $\{|00\rangle, |01\rangle, |10\rangle\}$. In the interaction picture and matrix form the above becomes

$$H = \hbar \begin{pmatrix} 0 & 0 & 0 \\ 0 & 0 & g \\ 0 & g & \Delta \end{pmatrix}, \quad (\text{S3})$$

$$\begin{aligned} \dot{\rho} = & -\frac{i}{\hbar}[H, \rho] \\ & -\frac{\Gamma_{1,Q}}{2} \begin{pmatrix} -2\rho_{22} & \rho_{12} & 0 \\ \rho_{21} & 2\rho_{22} & \rho_{23} \\ 0 & \rho_{32} & 0 \end{pmatrix} - \Gamma_{\phi,Q} \begin{pmatrix} 0 & \rho_{12} & 0 \\ \rho_{21} & 0 & \rho_{23} \\ 0 & \rho_{32} & 0 \end{pmatrix} \\ & -\frac{\Gamma_{1,D}}{2} \begin{pmatrix} -2\rho_{33} & 0 & \rho_{13} \\ 0 & 0 & \rho_{23} \\ \rho_{31} & \rho_{32} & 2\rho_{33} \end{pmatrix} - \Gamma_{\phi,D} \begin{pmatrix} 0 & 0 & \rho_{13} \\ 0 & 0 & \rho_{23} \\ \rho_{31} & \rho_{32} & 0 \end{pmatrix}, \end{aligned} \quad (\text{S4})$$

with ρ the density matrix, and $\Delta = \omega_T - \omega_Q$.

We are interested in the decay of the qubit excited state probability ρ_{22} , the relevant equations extracted from above are

$$\dot{\rho}_{22} = -ig(\overline{\rho_{23}} - \rho_{23}) - \Gamma_{1,Q}\rho_{22} \quad (\text{S5a})$$

$$\dot{\rho}_{23} = -ig(\rho_{33} - \rho_{22}) + i\Delta\rho_{23} - \Gamma\rho_{23} \quad (\text{S5b})$$

$$\dot{\rho}_{33} = -ig(\rho_{23} - \overline{\rho_{23}}) - \Gamma_{1,D}\rho_{33} \quad (\text{S5c})$$

with $\Gamma = \Gamma_{1,D}/2 + \Gamma_{\phi,D} + \Gamma_{1,Q}/2 + \Gamma_{\phi,Q}$.

In the limit $\Gamma_{1,D} > g$, $\rho_{33} \approx 0$, and we can approximate the system with two coupled differential equations. Inserting $\rho_{22} = \exp(-\Gamma_1 t)$ and $\rho_{23} = (\beta_r + i\beta_i)\exp(-\Gamma_1 t)$ gives

$$\Gamma_1 = 2g\beta_i + \Gamma_{1,Q} \quad (\text{S6a})$$

$$\Gamma_1\beta_r = \Delta\beta_i + \Gamma\beta_r \quad (\text{S6b})$$

$$\Gamma_1\beta_i = -g - \Delta\beta_r + \Gamma\beta_i, \quad (\text{S6c})$$

The solution for the qubit energy decay rate Γ_1 in the presence of a two-level defect is (for $\Gamma_{1,D} > g > \Gamma_{1,Q}$)

$$\Gamma_1 = \frac{2g^2\Gamma}{\Gamma^2 + \Delta^2} + \Gamma_{1,Q}. \quad (\text{S7})$$

MONTE CARLO SIMULATION OF DEFECTS IN THE XMON QUBIT

In order to quantitatively understand the Xmon qubit's energy decay as well as its variation over frequency, we have performed a Monte Carlo simulation for defects in the capacitor. The defect density for AlO_x in tunnel barriers has been established in measurements with phase qubits [4], with the distribution

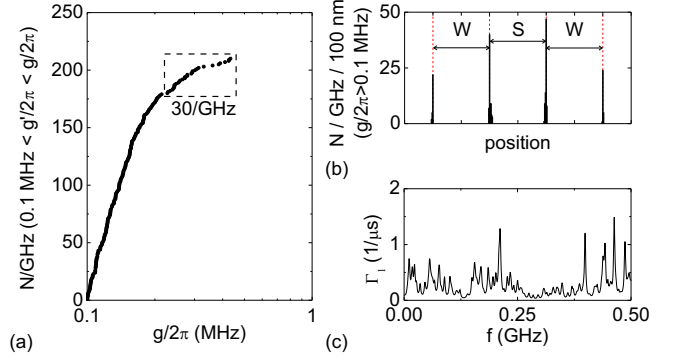


FIG. S5: (Color online) Monte Carlo simulation for defects in the Xmon capacitor, with $S=8$, $W=8 \mu\text{m}$ and the Xmon arm length $L=165 \mu\text{m}$. (a) Distribution of the defect coupling strength. A total of 210 defects/GHz have a coupling strength $g/2\pi > 0.1 \text{ MHz}$. A total of 30 defects/GHz have a coupling strength $g/2\pi > 0.22 \text{ MHz}$. (b) Distribution of the defects along position; number of defects in each 100 nm wide section is plotted. The cross section of the capacitor is dashed. (c) The simulated decay rate in a 0.5 GHz bandwidth using the distribution in (a,b), and Eq. S7.

over dipole moment p , volume, and frequency given by $\rho_0 \sqrt{1 - p^2/p_{\text{max}}^2}/p$, with $\rho_0 \approx 10^2/\mu\text{m}^3/\text{GHz}$, and the maximum dipole moment $p_{\text{max}} = 6 \text{ D}$. As the capacitor metal oxide and exposed substrate both consist of Al oxide, we assume that these numbers are a fair representation of the defect density in the qubit capacitor.

We randomly place defects, with the proper distribution over p , in a 3 nm thick dielectric layer ($\epsilon_r = 10$) on the substrate-air and metal-air interfaces (top metal surface as well as the etched edges). The substrate-metal interface is assumed to be thoroughly cleaned [1] and to contain no significant defect density. Using a thickness of 2 nm instead of 3 nm for the dielectric layer does not significantly influence the results. The coupling strength $g = pE$ is then calculated using a simulation for the electric fields in our geometry. The results are shown in Fig. S5.

In Fig. S5a, we have plotted the defect distribution over coupling strength. We find that, in a 1 GHz band, 30 defects have a coupling strength of $g/2\pi \gtrsim 0.2 \text{ MHz}$ (square). This simulated value is close to the experimentally observed density of $\sim 30/\text{GHz}$. These strongly coupled defects are predominantly located within a $\sim 100 \text{ nm}$ distance from the etched metal edges, including the exposed substrate surface close to the metal edges and capacitor metal oxide, where the electric fields are largest, see Fig. S5b.

The simulated qubit decay rate for the same defect distribution is shown in Fig. S5c in a 0.5 GHz bandwidth. For the defect decay rate we have assumed a uniform distribution based on the experimentally determined values: $1/\Gamma_{2,D} = 50 - 100 \text{ ns}$ ($\Gamma_{2,D} = \Gamma_{1,D}/2 + \Gamma_{\phi,D}$). The sim-

ulated decay rate reproduces both the peaks as well as the variation in the background which are observed in the measurement.



* These authors contributed equally to this work

† Present address: Department of Physics, Zhejiang University, Hangzhou 310027, China

[1] A. Megrant, C. Neill, R. Barends, B. Chiaro, Y. Chen, L. Feigl, J. Kelly, E. Lucero, M. Mariantoni, P. J. J. O'Malley, D. Sank, A. Vainsencher, J. Wenner, T. C.

- White, Y. Yin, J. Zhao, C. J. Palmstrøm, J. M. Martinis, A. N. Cleland, *Appl. Phys. Lett.* **100**, 113510 (2012).
- [2] Y. Chen, D. Sank, P. O'Malley, T. White, R. Barends, B. Chiaro, J. Kelly, E. Lucero, M. Mariantoni, A. Megrant, C. Neill, A. Vainsencher, J. Wenner, Y. Yin, A. N. Cleland, J. M. Martinis, *Appl. Phys. Lett.* **101**, 182601 (2012).
- [3] One Z unit corresponds to 0.5 mA in the control line on the chip.
- [4] J. M. Martinis, K. B. Cooper, R. McDermott, M. Steffen, M. Ansmann, K. Osborn, K. Cicak, S. Oh, D. P. Pappas, R. W. Simmonds, C. C. Yu, *Phys. Rev. Lett.* **95**, 210503 (2005).